Photodiagnosis and Photodynamic Therapy 25 (2019) 504–514

Contents lists available at ScienceDirect

Photodiagnosis and Photodynamic Therapy

journal homepage: www.elsevier.com/locate/pdpdt

Iron oxide/bismuth oxide nanocomposites coated by graphene quantum dots: "Three-in-one" theranostic agents for simultaneous CT/MR imaging-guided *in vitro* photothermal therapy

Samireh Badrigilan[a,b], Behrouz Shaabani[c], Nahideh Gharehaghaji[d], Asghar Mesbahi[e,*]

[a] Drug Applied Research Center, Tabriz University of Medical Sciences, Tabriz, Iran
[b] Department of Medical Physics, Faculty of Medical, Tabriz University of Medical Sciences, Tabriz, Iran
[c] Department of Inorganic Chemistry, Faculty of Chemistry, Tabriz University, Tabriz, Iran
[d] Department of Radiology, Faculty of Paramedical, Tabriz University of Medical Sciences, Tabriz, Iran
[e] Molecular Medicine Research Center, Biomedicine Institute, Tabriz University of Medical Sciences, Tabriz, Iran

ARTICLE INFO

Keywords:
Fe/Bi
Nanotheranostic
X-ray CT
MRI
Photothermal therapy
In vitro

ABSTRACT

Background: The all-in-one nanoprobes (NPs) have drawn biomedical attention in the cancer therapy field due to simultaneously combing the capabilities of therapeutic and diagnostic methods into a single nanoprobe.
Method: In this study, we developed a theranostic probe based on superparamagnetic iron oxide (SPIO) and bismuth oxide (Bi_2O_3) with graphene quantum dots (GQDs) coating to investigate the physical properties for *in vitro* CT/MR dual-modal biomedical imaging and cancer-specific photothermal therapy (PTT).
Result: The GQDs-Fe/Bi nanocomposites showed strong light absorbance profile with wide-band in the near-infrared region, without any sharp peak or decline. The highest photo-to-thermal conversion efficacy (η), was found to be 31.8% with the high photostability upon the irradiation of NIR 808-nm laser. The results of *in vitro* photothermal ablation of cancerous cells demonstrated that the cells significantly killed in the presence of NPs (~53.4%) with a dose-dependent manner in comparison to only laser group (3.0%). In GQDs-Fe/Bi nanocomposites, Bi with a high atomic number (Z = 83) exhibited a superior X-ray attenuation capability (175%) than the clinical CT agent-used dotarem, also, SPIO with excellent magnetization property showed strong T_2-relaxation shortening capability (r_2 = 62.34 $mM^{-1}.s^{-1}$) as a contrast agent for CT/MR imaging.
Conclusion: Our results demonstrate that the developed NPs can incorporate dual-modality imaging capability into a photo absorber for CT/MR imaging-guided tumor PTT.

1. Introduction

Nanomedicine has offered emerging techniques to achieve important objectives such as accurate diagnosis and treatment of cancerous tissues and reduce unwanted side effects [1]. In recent years, the introduction of theranostic nanosystems has been another revolution in cancer field that incorporates multimodal imaging techniques and therapeutic modalities into a single system [2–10]. Among these advancements, the theranostic method based on imaging-guided photothermal therapy (PTT) gained growing biomedical attention. To effective destroy cancer cells by PTT, the light harvesting exogenous nanoprobes are commonly used to effectively localize conversion of the near-infrared light (λ = 700–1100 nm) to heat within the exposed tissue [11–19]. The combination of multimodality imaging methods with PTT not only allow to diagnose of disease, but also provide the real-time observation to guide treatment process, selectivity therapy the target site, monitor the response of treatment, and enhance sensitivity and efficiency [12,20–25]. Among molecular imaging techniques, X-ray computed tomography (CT) has drawn considerable attention as the most effective and efficient modality for clinical abnormality diagnosis because it provides a three-dimensional (3D) image of the tissue with great spatial resolution and no depth limitation. Nevertheless, CT is not able to use for purposes of the targeted imaging and angiography due to short blood circulation half-life and non-specific extracellular distribution, known as pharmacokinetic properties, of common CT contrast agents based on small iodinated molecules. In addition, CT imaging with inherent defects failures to distinguish different soft tissues that own very close mass densities to each other. Nevertheless, a combination of CT with another imaging methods not only allow to profit the entire benefits of two imaging methods, but also overcome

* Corresponding author at: Department of Medical Physics, Faculty of Medical, Tabriz University of Medical Sciences, Tabriz, Iran.
E-mail address: amesbahi2010@gmail.com (A. Mesbahi).

https://doi.org/10.1016/j.pdpdt.2018.10.021
Received 9 August 2018; Received in revised form 25 October 2018; Accepted 26 October 2018
Available online 29 October 2018
1572-1000/

the shortcomings of the both which is more desirable for the accurate diagnosis since the single method is not adequate to accurate abnormality diagnosis and acquire comprehensive and useful structural information.

For clinical CT imaging, the powerful magnetic resonance imaging (MRI) technique has introduced as an effective complement with respect to the non-ionizing radiation source and excellent soft tissue contrast. Thus, the CT/MR dual imaging is reasonable to take all the necessary information and precision diagnose.

In recent years, nanoparticles (NPs) based on Bi compounds such as Bi_2S_3 and Bi_2Se_3 have employed as effective photothermal and contrast agent for PTT and CT imaging [4,11,26–34]. The CT contrast directly dependent on the atomic number of active elements and their concentration. Bi-metal with high atomic number (Z = 83) hold a higher X-ray attenuation coefficient than other commonly the developed CT nanoagents (I: 1.94; Ta: 4.30; Au: 5.16; Pt: 4.99; Bi: 5.74 $cm^2.g^{-1}$ at 100 keV). Therefore, pure Bi NPs reveal a larger contrast enhancement efficacy in CT images, due to its higher Bi payload in comparison to the Bi compounds [2,12,35]. Therefore, Bi as the most biocompatible heavy metal and cost-effectiveness features has attracted growing interest in CT imaging.

Furthermore, the Bi chalcogenides (Bi_2E_3, E = S and Se) with direct bandgap show a high light absorption in NIR region, and great photo-to-thermal conversion capability, which made it possible to be used to cancer-specific therapy of photothermal. In recent years, the photothermal agents based on pure Bi NPs with higher or comparable photothermal efficiency have introduced as a better choice, importantly, they have no need for toxic synthetic reagents and complex processes. The recent studies reported that the use of Bi nanoagent for CT image-guided PTT have allowed to accurately localize and treat the tumors within soft tissues [2,12]. In another side, according to the superparamagnetic behavior, the iron oxide nanoparticles (Fe_3O_4 NPs) are used as negative contrast agents in T_2-weighted MRI. Thus, the Fe/Bi nanocomposites are able to effectively guide PTT for cancer treatment with respect to the excellent capability of Bi and Fe NPs for CT and MR imaging, which successfully harvest the advantages of diagnostic and therapeutic methods within a single theranostic nanoprobe. The $FeSe_2$/Bi_2Se_3 theranostic nanostructure showed great potential for CT/MR imaging-guided photothermal therapy [29]. To date, the research on developing simultaneously Bi and Fe NPs as a theranostic platform for CT/MR imaging and PTT have not been reported previously. In another side, graphene NPs and its derivatives exhibit satisfactory biocompatibility, strong optical absorbance and photo-stability in biomedical applications, also, significantly prevent the NPs agglomeration in a biological environment [11]. Therefore, in the present study, we synthesized Fe/Bi nanocomposites with a biocompatible coating of graphene quantum dots (GQDs) (Fig. 2A). We also evaluated the ability of GQDs-Fe/Bi NPs to enhance CT and MR imaging contrast and induce therapeutic effect by converting photo-to-thermal energy upon near-infrared laser irradiation. Such theranostic agent not only shows strong near-infrared (NIR) absorbance, but also offers high-contrast bi-modality imaging to CT/MR imaging-guided PTT for early cancer treatment (Scheme 1).

2. Material and methods

2.1. Fabrication of hybrid nanoparticles

Materials: Iron(III) Chloride hexahydrate ($FeCl_3.6H_2O$), Iron(II) Sulfate heptahydrate ($FeSO_4.7H_2O$), sodium hydroxide (NaOH), ammonium hydroxide ($NH_3.H_2O$), nitric acid (HNO_3), urea, sulfuric acid (H_2SO_4) and potassium nitrate (KNO_3) were purchased from Merck and citric acid and Bismuth (III) Nitrate pentahydrate (Bi $(NO_3)_3.5H_2O$) were purchased from Sigma.

2.1.1. Synthesis of the graphene quantum dots (GQDs)

The product of graphene quantum dots (GQDs) was synthesized by a one-step method using pyrolysis of citric acid as follows [36]:

Three grams of citric acid were dissolved in double distilled water, and then were heated and melted. It kept for 30 min followed by the solution color change into dark orange. 1.5 M solution of NaOH was drop-wise added in the above solution in room temperature.

2.1.2. Synthesis of the GQDs coated Fe_3O_4 nanoparticles

GQDs coated Fe_3O_4 NPs were prepared as follows: $FeCl_3$-$6H_2O$ (1.18 g) and $FeSO_4$-$7H_2O$ (0.82 g) were dissolved in 5 ml de-ionized water. In another side, 5 ml of the prepared GQDs solution were adjusted to 7 pH by ammonium hydroxide then the above solution was added under nitrogen flow with vigorous stirring and heated to 80 °C. After 20 min, 10 ml of ammonium hydroxide were rapidly added to the solution. The final suspension was obtained after 90 min.

2.1.3. Synthesis of the Fe/Bi nanocomposites

$FeSO_4.7H_2O$ (0.452 g) and $FeCl_3.6H_2O$ (0.678 g) were dissolved in 20 ml de-ionized water under nitrogen gas with vigorous stirring at temperature room. Then 20 ml of ammonium hydroxide were added the solution. After the solution was fully dissolved, then Bi (NO_3) $0.5H_2O$) 0.23 g) also was added. The final solution slowly was brought to 90 °C and maintained for 3 h under nitrogen flow.

2.1.4. Synthesis of the GQDs-Fe/Bi nanocomposites

For coating Fe/Bi NPs, 10 ml of GQDs were adjusted to 7 pH with ammonium hydroxide under magnetic stirring for 15 min. The as-prepared Fe/Bi NPs was added to the GQDs solution and stirring for 20 min. Then the temperature of a mixture solution of Fe/Bi NPs and GQDs was increased to 60 °C for 1 h.

2.2. Characterization

The morphology and size of the prepared NPs were characterized by field-emission scanning electron microscopy (MIRA3/TESCAN-XMU, USA) and transmission electron microscopy. The hydrodynamic size and size distribution of particles were determined by Nano S zeta-sizer (Malvern Instruments, Malvern, UK). Fourier transform infrared (FTIR) spectra were performed by an FT-IR spectrophotometer (Tensor27, Bruker, Germany) using KBr pellets. The microstructural characterization was investigated by an X-ray diffractometer (PANalytical XPert-pro) with the Cu-Kα radiation. The determination of the elemental concentration of Fe and Bi were obtained using flam atomic absorption spectrometer (NovAA 400, Analytik Jena, Germany). Magnetic property was examined via a vibrating sample magnetometer (MDKFT, Iran). Surface plasma resonance property was carried out by a UV–vis-NIR spectrophotometer (UV–Vis, USA).

2.2.1. Measurement of photothermal performance

To study the photothermal performance, the GQDs-Fe/Bi NPs suspension with a series of concentration of active Bi-metal (0, 50, 100, 175, 250 $\mu g.mL^{-1}$) were irradiated with a NIR laser (808 nm, 1.7 $W.cm^{-2}$) for 10 min and the solution temperature was monitored every 1 s by a thermocouple thermometer (thermometer Standard ST-612) with an accuracy of ± 0.1 °C. To measure the photothermal conversion efficiency (η), a fixed concentration (250 μg Bi. mL^{-1}) of GQDs-Fe/Bi NPs suspension was exposed to an 808-nm laser (1.7 $W.cm^{-2}$) to the point, where the temperature change of the solution was negligible and reached a constant state. Afterward, the laser radiation was interrupted to allow the solution to undergo naturally a cooling phase to ambient temperature. To study the photo-to-thermal conversion stability, the three cycles of heating and cooling phase of GQDs-Fe/Bi NPs suspension (250 μg Bi·mL^{-1}) under a laser irradiation (808 nm, 1.7 $W.cm^{-2}$, 20 min) were monitored.

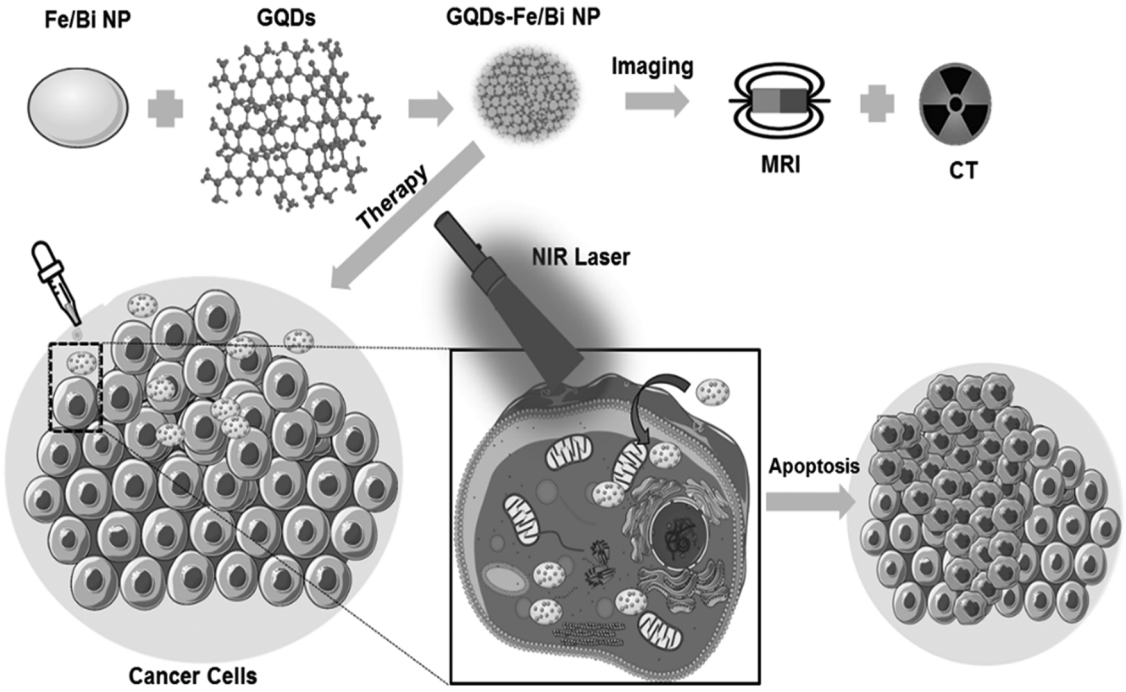

Scheme 1. Schematic illustration of GQDs-Fe/Bi NPs as a theranostic agent for simultaneous MR/CT imaging- guided photothermal therapy.

2.2.2. CT & MR imaging

2.2.2.1. Magnetic resonance (MR) imaging. To perform phantom MR imaging and relaxivity studies, various concentrations of GQDs-Fe/Bi NPs and GQDs-Fe_3O_4 NPs were dispersed in de-ionized water. All experiments were performed on a 1.5 T MR system (Siemens Avanto-Germany). The longitudinal (T_1) and transverse (T_2) relaxation times of MR agents were measured using a spin echo sequence, and relaxation times were measured using a multi spin echo sequence. The longitudinal (r_1) or transverse (r_2) relaxivities, as the efficiency of nanoprobes, were obtained from the slope of the linear plot of $1/T_1$ or $1/T_2$ against the Fe concentrations (0, 0.0625, 0.1075, 0.1433, 0.2238 mM), respectively. The instrumental parameters of a T_1 and T_2-weighted MRI were adjusted as follows:

For T_2-weighted imaging:

TR = 3000 ms, TE = 13–121 ms, FA = 90°, slices thickness = 5 mm.

For T_1-weighted imaging:

TR = 250-500-1000-2000-3000 ms, TE = 11 ms, FA = 90°, slices thickness = 5 mm.

2.2.2.2. X-ray CT imaging. In order to acquire CT images, the GQDs-Fe/Bi NPs and urografin 76% (an iodine-based conventional CT agent) at different concentrations (0, 0.5, 1, 1.5, 2 and 2.4 mg) were dispersed in de-ionized water. CT imaging was carried out to determine X-ray attenuating capability of each sample using a multidetector CT scanner (GE HiSpeed).

Imaging parameters were as follows: slice thickness = 5 mm, Pitch = 1.5, 80–140 kV, 150 mA.

Hounsfield unit (HU) was considered as the contrast enhancing efficiency of contrast agents.

2.2.3. In vitro hemolysis assay

A fresh blood sample was firstly stabilized by Ethylene Diamine Tetraacetic Acid (EDTA) and human red blood cells (HRBCs) were separated by removing the plasma via centrifuge at 1000 rpm for 10 min. Then HRBCs were purified by five sequential washing and 10-fold diluted with phosphate buffered saline (PBS). Afterward, 300 µL of the diluted HRBC suspension were added to 1.2 ml of deionized water (as a positive control), 1.2 ml of PBS (as a negative control) and 1.2 ml of PBS containing different concentrations of the GQDs-Fe/Bi NPs and GQDs-Fe_3O_4 NPs ranging from 100, 200, 350 and 500 µg.mL^{-1}, respectively. The samples gently were mixed and then incubated for 2 h at room temperature without moving. Subsequently, the samples were centrifuged at 10,000 rpm for 2 min. Finally, a UV − vis spectrophotometer (BDSL Immunoskan MS, Finland) was used to measure the hemoglobin absorbance of supernatants at 541 nm. The hemolysis capability of NPs was calculated using the following equation:

$$\text{Percent Hemolysis (\%)} = \frac{A_{test} - A_{negative}}{A_{positive} - A_{negative}} \times 100\% \quad (1)$$

Where A_{sample} is the absorbance of sample. $A_{positive}$ and $A_{negative}$ is the absorbance of positive control and negative control, respectively.

2.2.4. Cell cytotoxicity assay

HeLa (human cervical carcinoma cell) and MCF-7 (human breast carcinoma cell) cells were chosen to perform cellular cytotoxicity assay. The cells were cultivated in 25 cm^2 plates in RPMI 1640 medium (gibco ®) containing 10% (v/v) fetal bovine serum (Sigma), penicillin (100 U/mL) and streptomycin (100 U/mL) (gibco ®) under humidified atmosphere with 5% CO_2 at 37 °C and they were in the exponential phase of growth for the duration of the whole experiment. The MTT test was performed on both types of cancerous cells to quantify their viability after treatment with the GQDs-Fe/Bi NPs and GQDs-Fe_3O_4 NPs at different concentrations (0, 100, 200, 350, 500 µg.mL^{-1}, respectively). Firstly, both the HeLa and MCF-7 cells were seeded into 96-well cell culture plates with a density of $\sim 10 \times 10^3$ in triplicate and incubated for 24 h to reach appropriate confluency. Then the primary medium was substituted with new medium containing the NPs with different concentrations and a pure medium (as control). After second incubation for 24 h, 20 µL of 3-(4,5-dimethylthiazol-2-yl)-2, 5-diphenyltetrazolium bromide (MTT, Roche) solution (5 mg.mL^{-1}) were added to each well and cells further incubated for 4 h at 37° until a purple precipitate was observable. Next, the medium was replaced with 150 µL of dimethyl sulfoxide (DMSO) in order to dissolve the formazan crystals. The cell viability percentages of samples were measured as follows:

$$\text{Cell viability}\ (\%) = \frac{OD_{test}}{OD_{control}} \times 100 \quad (2)$$

Where $OD_{control}$ and OD_{test} are the optical absorptions of cells treated with PBS and NPs, respectively.

Subsequently, the optical absorptions were measured by a microplate spectrophotometer (EPOCH, USA) at 570 nm to determine the relative number of viable cells.

2.2.5. In vitro PTT on Cancer cells

To investigate the photo-to-thermal conversion efficiency, an 808 nm laser with 1.7 w/cm^2 power density was employed to irradiate the aqueous dispersions of GQDs-Fe/Bi NPs at a range concentration of active metal (0, 50, 100, 175, 250 Bi μg. mL^{-1}). A thermocouple thermometer (thermometer Standard ST-612) was used to record the solutions temperatures after laser radiation with an accuracy of ± 0.1 °C every 60 s.

Moreover, to study photothermal therapy effect of the GQDs-Fe/Bi NPs at the cellular level, HeLa and MCF-7 cells were cultivated in 96-well plates (~ 1×10^4 cells per well) for 24 h and two types of cells were divided into three groups. After 24 h, the culture medium was changed and the cells in the last group were incubated with different doses (25, 50, 75, 100 μg.mL^{-1}) of the GQDs-Fe/Bi NPs suspensions.

After 12 h, no treatment was used for the first groups. The second ones were only exposed to the laser (808 nm, 1.7 W.cm^{-2}) for 10 min. The third ones (treated with GQDs-Fe/Bi NPs) were irradiated with laser (808 nm, 1.7 W.cm^{-2}) for 10 min. After another 1 h, the standard MTT method, like the previous section, was used to measure the cell viability in each group. The photothermal assay was repeated three times for each group. In addition, a light microscope (OPTIKA XDS-3, Italy) was used to observe changes in cells morphology induced by GQDs-Fe/Bi NPs upon NIR laser. Moreover, the possible mechanism of dead cell after photothermal therapy was investigated by the flow cytometry analysis as follows: 5×10^5 Cells were treated with different concentrations of GQDs-Fe/Bi NPs (0,25,50,75,100 μg.mL^{-1}), then adherent and detached cells were collected, centrifuged at 200*g for 5 min and then resuspended in annexin-v labeling solution (prepared as protocol of Roche annexin-v –FLUOS staining kit), mixed and incubated for 10–15 min at 25 °C temperature.

2.3. Statistical analysis

The results are presented as mean ± standard deviation. One-way analysis of variance and/or Student's *t*-test were used to analyze the differences between several groups, $p < 0.05$ was considered statistically significant difference. All the graphs and statistical analysis were performed using GraphPad prism Ver.7.03. Apoptosis results were analyzed by FlowJo Ver.10.

3. Results and discussion

3.1. Characterization of nanoparticles

The FT-IR spectra of as-synthesized NPs were displayed in Fig. 1**A**. The bands at about 3200 cm^{-1} and 3430-3440 cm^{-1} range indicated the hydroxyl groups (O- H) of the GQDs. The strong vibrational bands at about 1700 and 1200-1400 cm^{-1} were corresponding to C=O carboxyl or carbonyl stretching vibrations, O−H deformation of the C − OH group in GQDs. in addition, the appeared bands between 1000-1100 cm^{-1} correspond to C − O asymmetric stretching vibration of epoxide in GQDs. To this point, all the mentioned bands confirmed the presence of oxygen-containing functional groups on GQD surface. The strong vibrational bands at 1500 to 1650 cm^{-1} were related to the presence of C=C stretching vibration bands of graphitic skeleton (sp^2) domains. The appeared bands in IR spectrum around of 500 to 600 cm^{-1} indicated the bonding of metal to oxygen atoms of groups on the GQDs surface. Due to the GQDs surface has negative charges and oxygenated species, the positive ions of metal (III) such as Bi^{3+} and Fe^{3+} can easily be bonded to the surface of GQDs. In addition, the surface of GQDs has hydrophilic groups such as −OH and −COOH, which mainly contribute to their excellent water solubility. The XRD pattern (Fig. 1**B(a)**) could be well-indexed to the cubic structure of Fe_3O_4 (JCPDS: 96-900-5814) with diffraction peaks at 30.2°(220), 35.59°(311), 43.27°(400), 53.68°(422), 57.21°(511) and 62.84°(440), and the XRD pattern of Fe/Bi NPs (Fig. 1**B(b)**) indicated the Bi rhombohedra structure (JCPDS: 96-900-8577) with diffraction peaks at 22.48° (003), 27.2° (012), 37.96° (104), 39.62° (110), 44.49° (015), 45.91° (113), 48.715° (202), 56.104° (024) and 64. 523° (122) and Fe_3O_4 cubic structure. The loops of the curves (Fig. 1C) verified the super paramagnetic nature of the as-prepared NPs. The bare Fe_3O_4 NPs indicated saturation magnetization (M_s) value of 75.41 emu/g. However, this value for GQD-Fe_3O_4 NPs reduced to 61.22 emu.g^{-1}, confirming successful coating of GQDs on the surface of NPs. The magnetization value of GQDs-Fe/Bi NPs was 48.59 emu/g, due to the diamagnetic behavior of Bi. However, these NPs still exhibited good magnetic property.

According to the TEM image, the size of GQDs was found to be smaller than 5 nm (Fig. 2**B**). In addition, the average diameter of Fe/Bi nanocomposites was measured about 64 ± 5.46 nm using TEM (Fig. 2**C**) and SEM (Fig. S1.A) images. It should be noted that magnetite and bismuth hydroxide possess a very close density of each other with values of 5.1 g.cm^{-3} and 4.96 g.cm^{-3}, respectively. According to this, the Fe/Bi nanocomposite was found to be homogeneous using the typical transmission electron microscopy. In TEM image, it was clear that Fe/Bi nanocomposites located in the core and the GQDs with very lower density formed the shell of GQDs-Fe/Bi nanosystem. In addition, the size of Fe_3O_4 NPs was determined to be 21 nm using a SEM (Fig. S1.B). The hydrodynamic size of GQDs-Fe/Bi nanocomposites and GQDs-Fe_3O_4 NPs were shown in Fig. S1.C–D. The polydispersity indexes (PDI), as the degree of distribution non-uniformity, for GQDs-Fe/Bi NPs and GQDs-Fe_3O_4 NPs were 0.3 and 0.19, respectively. The hydroxyl/carboxyl groups on the hydrophilic surface of NPs in the aqueous solution absorbed water molecules, owing to their diameter size in TEM and SEM were different from DLS.

3.1.1. In vitro MR imaging

MR Contrast probes do not directly improve the contrast of the images, unlike radionuclide, optical harvesting, and X-ray attenuating probes [37]. They affect the intensity of the signal by reducing the longitudinal (spin-lattice) and transverse (spin-spin) relaxation times of the neighboring water protons. The MR contrast enhancing ability of GQDs-Fe_3O_4 NPs and GQDs-Fe/Bi NPs were measured for the various concentrations of Fe. As displayed in Fig. 3**. A**, more brightness was observed for the T_1-weighted images as the concentration increased. In addition, such obvious signal intensity amplification with the increase of Fe concentrations was measured by quantifying the brightness degree, indicating a positive contrast effect. The growth of the longitudinal relaxation rate ($1/T_1$) of protons in NPs aqueous solution linearly was dependent on the Fe concentration (Fig. 3**B**). The relaxivity (r) is introduced as a key parameter to evaluate the performance of the contrast agent. It is deduced from linear plotting the T relaxation rate (1/T) against of the concentration as follows:

$$\frac{1}{T} = \frac{1}{T^0} + RC \quad (3)$$

For the T_1-weighted image, 1/T and 1/T° referred to the obtained longitudinal relaxation rate of the samples in the presence and absence of CAs, respectively; R and C are longitudinal relaxivity and concentration of the agent sample, respectively. The longitudinal relaxivity (r_1) value for the GQDs-Fe_3O_4 NPs and QGDs-Fe/Bi NPs were calculated to be 1.89 mM^{-1}.s^{-1} and 2.37 mM^{-1}.s^{-1}, respectively (Fig. 3**. B).** In contrast, on evaluating the T_2-weighted images, the brightness of images diminished proportionally to the Fe concentration, indicating

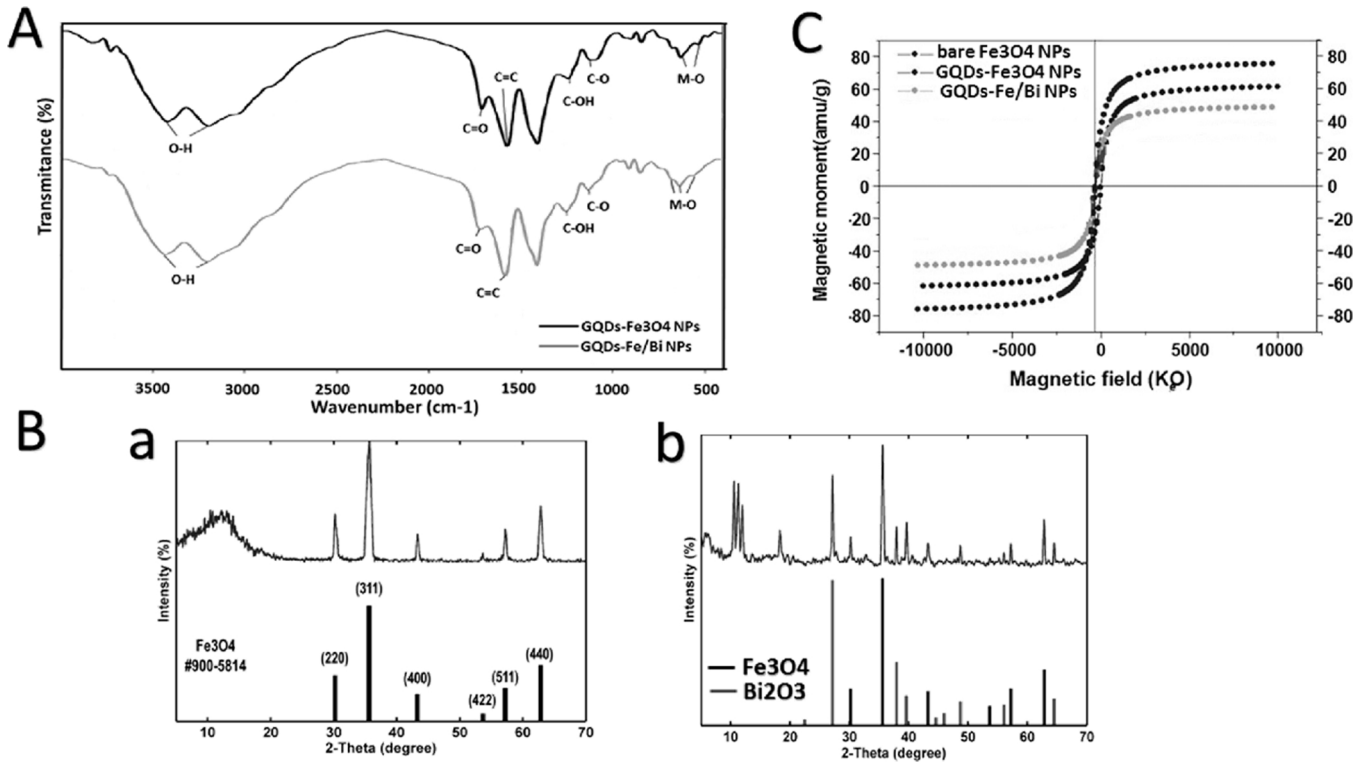

Fig. 1. A) FTIR patterns of GQDs-Fe_3O_4 NPs and GQDs-Fe/Bi NPs; **B)** X-ray diffraction pattern of a) GQDs-Fe_3O_4 NPs, b) GQDs-Fe/Bi NPs; **C)** Magnetization curve of bare Fe_3O_4 NPs, GQDs-Fe_3O_4 NPs and GQDs-Fe/Bi NPs.

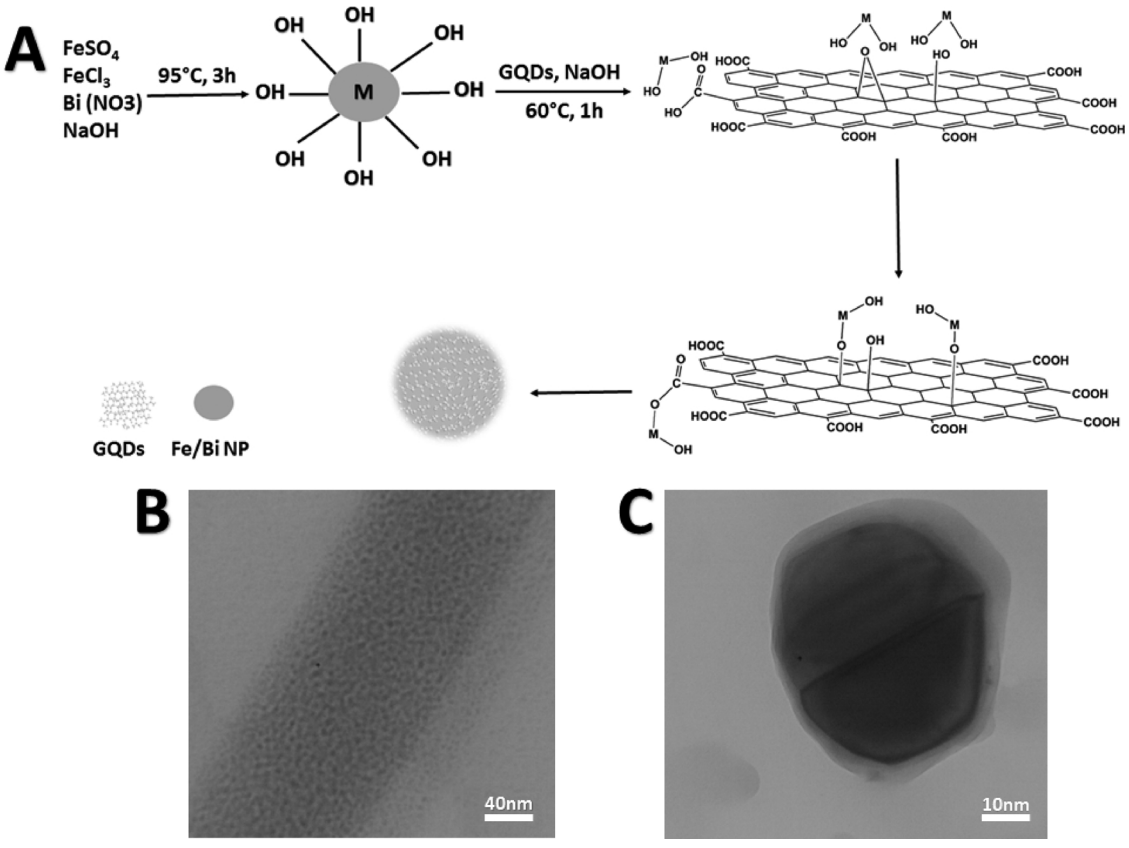

Fig. 2. A) Illustration of GQDs-Fe/Bi NPs synthesis strategy; TEM images of **B)** GQDs and **C)** GQDs-Fe/Bi NPs.

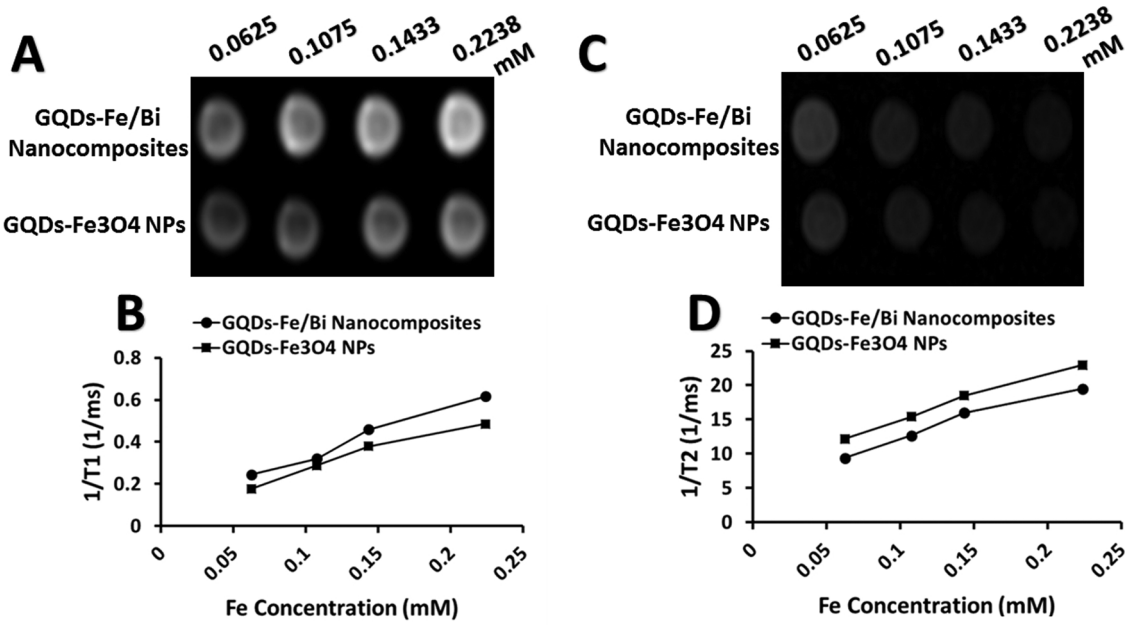

Fig. 3. MR imaging performance: **A)** T_1-weighted MR images and of **B)** The T_1 relaxation rate of GQDs-Fe_3O_4 NPs and GQDs-Fe/Bi NPs with different concentration of Fe; **C)** T_2-weighted MR images and of **D)** The T_2 relaxation rate of GQDs-Fe_3O_4 NPs and GQDs-Fe/Bi NPs with different concentration of Fe.

the behavior of the Fe_3O_4 as a negative contrast agent. In another word, the Fe-based NPs acted as image darkening agent, causing the reduced signal intensity (Fig. 3**.C**). According to the Eq. (3), the QGDs-Fe_3O_4 NPs showed a high transverse relaxivity (r_2) with a value of 66.52 $mM^{-1}.s^{-1}$. In contrast, the r_2 value of GQDs-Fe/Bi nanocomposites decreased to 62.34 $mM^{-1}.s^{-1}$ **(**Fig. 3**. D).** The obtained results were in agreement with their measured magnetization property, taken into the account that the T_2 relaxivity owns a direct relationship with the saturation magnetization of the NPs. The difference between the obtained results for GQDs-Fe_3O_4 NPs and GQDs-Fe/Bi nanocomposites can be ascribed to the diamagnetic behavior of Bi, which mainly decreases of magnetization property, subsequently their transverse relaxivity magnitude. In should be noted although the measured transverse relaxivities (r_2) of contrast agents in our study were smaller than that of the reported for the FeBi@SiPEG core-shell nanocrystals (175 $mM^{-1}.s^{-1}$) [38] and $FeSe_2$ -Decorated Bi_2Se_3 nanosheets (138.46 $mM^{-1}.s^{-1}$) [29], but their contrast-enhancing capability were comparable to Bi/Fe_3 nanocomposites (Fe-70, Bi-30; 68 $mM^{-1}.s^{-1}$) [39] and were considerably greater than that of the MnSe (27.6 $mM^{-1}.s^{-1}$) [27] and MnS (24.08 $mM^{-1}.s^{-1}$) [40] cores encapsulated inside in Bi2 × 3 (X = S or Se) shell nanostructure. Moreover, the effective shortening ability of T_2 relaxation of surrounding water protons induced by GQDs-Fe/Bi nanocomposites was comparable to the common dual agents based on Au/Fe e.g. the Fe_2O_3@Au Core@ Shell nanoparticles (56.12 $mM^{-1}.s^{-1}$) and the Fe_3O_4@Au nanocomposites (71.55 $mM^{-1}.s^{-1}$) [41,42]. The capability of a given material as positive (T_1) or negative (T_2) contrast agent was examined by calculating the r_2/r_1 ratio. The GQDs-Fe_3O_4 NPs and the GQDs-Fe/Bi nanocomposites offered r_2/r_1 ratios of 35.196 and 26.23, respectively. The relatively high r_2 or high r_2/r_1 value reveal that QGDs-Fe/Bi NPs can able to serve as an effective negative contrast agent in T_2-weighted MR imaging.

3.1.2. *In vitro CT imaging*

According to the strong x-ray attenuating capability of the Bi element, it was anticipated that the GQDs-Fe/Bi NPs also can act as a good CT agent. To investigate attenuating property, the CT images of different concentration of GQDs-Fe/Bi NPs were acquired. As shown in Fig. 4**.A.** the CT images become gradually brighter with the increasing of active element concentration of Bi, where the image brightness represents the magnitude of CT signal intensity. In addition, a linear amplification of the CT values (HU) was observed with the concentration. The GQDs-Fe/Bi NPs produced much higher Hounsfield units (230 HU) than the small molecules iodine (134 HU) at the highest concentration **(**Fig. 4**. B).** A concentration of 1 $mg.ml^{-1}$ GQDs-Fe/Bi NPs provided an equivalent X-ray attenuation (120 HU) as urografin contain of 2 $mg.ml^{-1}$ iodine. This high X-ray absorption corresponded to the strong attenuation of X-rays in bismuth (Bi: 5.74, 1.96 $cm^2.kg^{-1}$ in 100Kev) and partly to Fe element, which caused an effective atomic number of Z = 106, according to the following equation:

$$\bar{Z} = \sqrt[2.94]{2 \times Z_{Bi}{}^{2.94} + 3 \times Z_{Fe}{}^{2.94}} \quad (4)$$

This corresponded that the CT contrast enhancement efficiency of the GQDs-Fe/Bi NPs (44.4 HU. mM^{-1}) was a nearly 1.7 fold as that of urografin (25.35 HU. mM^{-1}). The contrast efficiency is deduced from the slope of linear Hounsfield units (HU) curve as function of concentration (mg). As shown in Fig. 4**. C,** the CT imaging performance of GQDs-Fe/Bi NPs also was evaluated at commonly used X-ray tube voltages (80, 120 and 140Kv). The GQDs-Fe/Bi NPs displayed higher pronounced X-ray attenuating ability at 80 kV corresponds to the position of bismuth's K edge (90.8 Kev), which was consistent with previous results reported for Bi NPs. [39,43] In this voltage, the CT contrast enhancement was about 22% higher than those of the reported for the other tube voltages. For GQDs-Fe/Bi NPs, there was no difference between the measured x-ray attenuation magnitude at voltages of 120 kV and 140 kV, while a sharper HU value reduction was recorded for iodine. The obtained results demonstrated that GQDs-Fe/Bi NPs can be ideal to achieve a similar contrast using any protocol CT imaging.

3.1.3. *In vitro Cytotoxicity*

Blood compatibility has been considered as one of the vital test and the key factors in studies of NPs before in vivo biomedical applications. Hemolysis is defined as the response of blood to exogenous materials which give rise to the release of their cytoplasm and hemoglobin into surrounding fluid. The hemolytic activity induces side effects such as anemia, hypertension, and renal toxicity. As shown in Fig. 5**.A**, the hemolysis degree highlighted as a function of NPs concentration, however, the highest value was calculated to be less than 2% even at the concentration of 500 $\mu g.ml^{-1}$. According to the criterion of ASTM

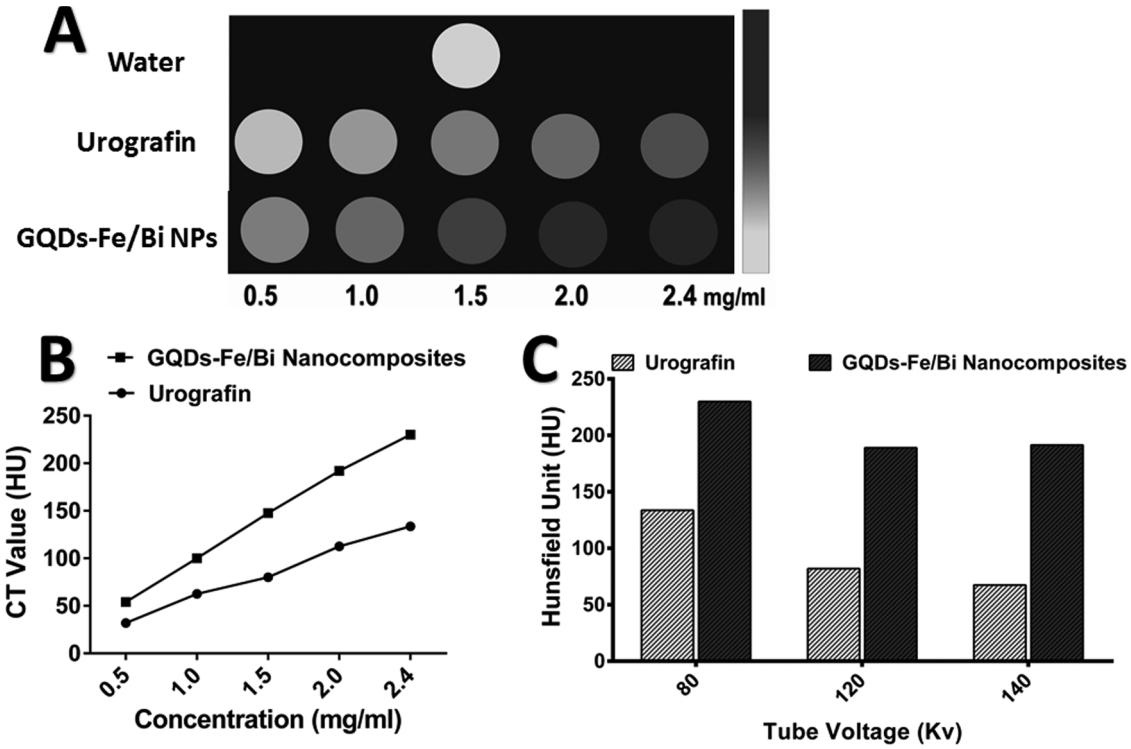

Fig. 4. CT imaging performance: **A)** CT images of urografin and GQDs-Fe/Bi NPs with different concentration of Bi; X-ray attenuation intensity (HU) as a function **B)** of the Bi element concentration and **C)** of X-ray tube voltages (80 − 140 kV).

E2524-08 standard, the role of agents as the RBCs damager highlight when the degree of hemolysis is more than 5% [44]. The toxicity of the developed NPs is an important issue for further applications in biomedical purposes. In this regard to get a reliable result, the cytotoxicity effects caused by the uptake of NPs were evaluated. As shown in Fig. 5**.B-C**, a dose-dependent survival reduction was observed upon exposing both types of cell lines to NPs. These results showed a cellular compatibility of the as-synthesized NPs.

3.1.4. NIR photothermal properties

The GQDs-Fe/Bi NPs revealed a strong UV–vis–NIR absorbance profile with any sharp peak or decline (Fig. 6A). Therefore, the PTA in

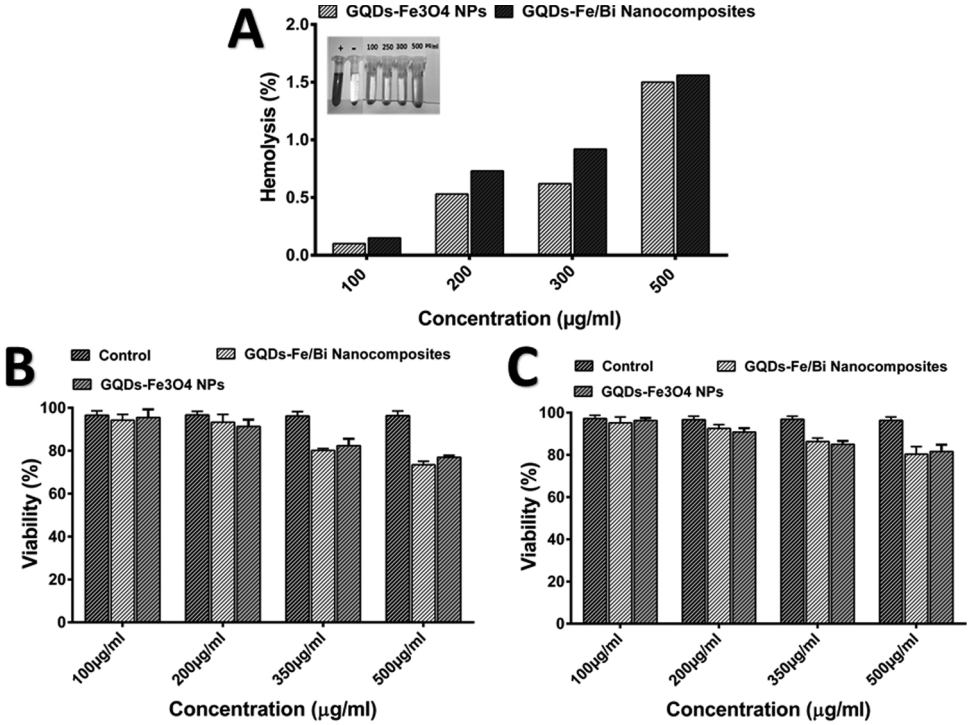

Fig. 5. A) Hemolytic percentage of RBCs incubated with GQDs-Fe_3O_4 NPs and GQDs-Fe/Bi NPs as a function of concentration; **B–C)** Cell viability of MCF-7 (B) and HeLa (C) after incubation with different concentrations of GQDs-Fe_3O_4 NPs GQDs-Fe/Bi NPs for 24 h using standard MTT assay.

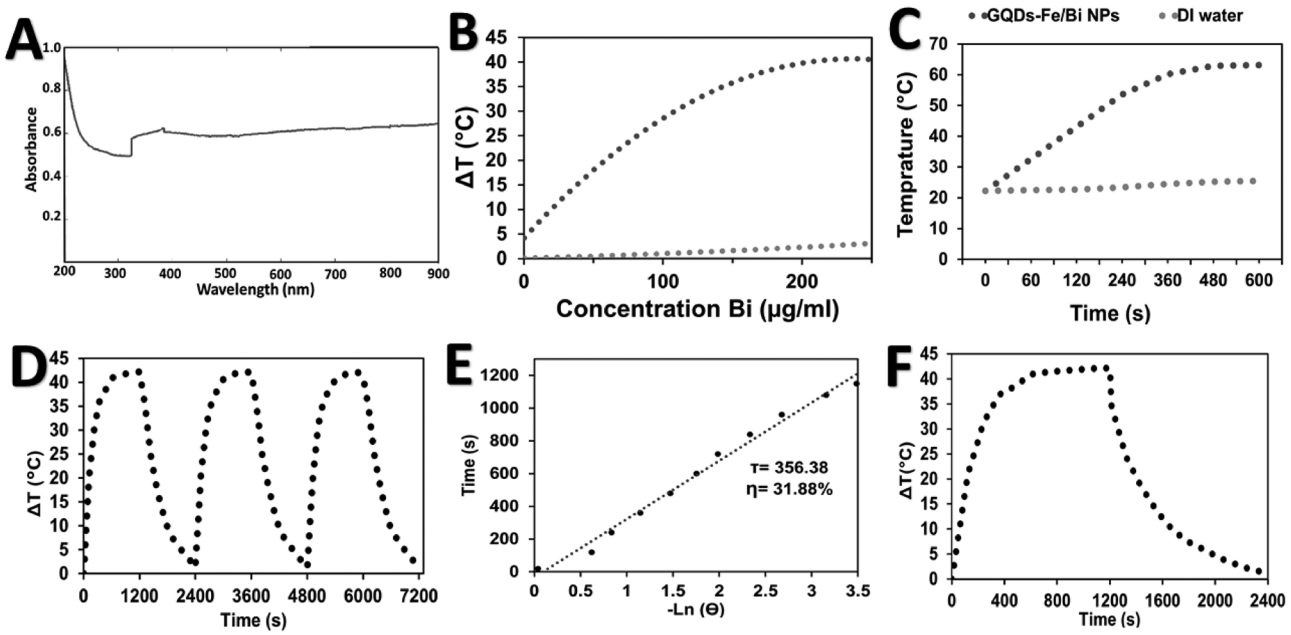

Fig. 6. Photothermal Property: **A)** UV–vis-NIR absorbance spectra of GQDs-Fe/Bi Nanocomposites; Temperature elevation of water and the GQDs-Fe/Bi NPS aqueous solutions as function of **B)** concentration and **C)** irradiation time; **D)** Temperature variations of the GQDs-Fe/Bi NPs (250 ppm of Bi) during three cycles of heating and cooling phase; **E)** The photothermal response of GQDs-Fe/Bi NPs (250 ppm of Bi); **F)** Determination of the time constant of the GQDs-Fe/Bi NPs aqueous solution (250 ppm of Bi) for heat transfer from the system using a linear regression of the cooling profile of GQDs-Fe/Bi NPs.

our study may be promising for broadband PTT applications, and the superiority may become more pronounced when the irradiation wavelength is larger (> 800 nm).

To study the photo-to-light conversion efficiency, a gradient concentrations of GQDs-Fe/Bi NPs dispersions (0, 50, 100, 175, 250 $\mu g.ml^{-1}$) was exposed to the 808 nm laser for 10 min. As displayed in Fig. 6**B-C**, the temperature of the NPs dispersions rapidly raised with an active metal concentration- and irradiation time-dependent manner.

For example, a temperature elevation (ΔT) of 15 °C was recorded for the concentration of 50 $\mu g.ml^{-1}$ upon 10 min laser irradiation. Take into account that normal tissue temperature is about 37 °C, the GQDs-Fe/Bi NPs hypothetically can rapidly raise the temperature of targeted tissue over 50 °C, which it is considered as cell killing temperature [4,26,45]. In contrast, the control sample showed only a slight increase of about 3.2 °C. The photothermal stability, as a key property of photothermal agents, was examined for three cycles of heating and cooling phase under the same irradiation condition (250 $\mu g.ml^{-1}$, 20 min, 1.7 $W.cm^{-2}$). Their temperature changes in the repeated cycles were insignificant for the GQDs-Fe/Bi NPs, indicating their excellent photostability properties after laser irradiation (Fig. 6D). The photo-to-thermal conversion efficiency (η) was measured to quantitatively evaluate the photothermal performance of the GQDs-Fe/Bi NPs. Thus, a fixed concentration of each PTAs (250 $\mu g.ml^{-1}$) was exposed with NIR laser with a continuous time of 20 min (Fig. 6E), and then followed a cooling phase to room temperature naturally for the same time (20 min). The photothermal performance of NPs was calculated using the following equation:

$$\eta = \frac{hS(T_{max.NPs} - T_{max.water}) - Q_0}{I(1 - 10^{-A_\lambda})} \quad (5)$$

$$\mathbf{hS} = \frac{\sum \mathbf{mCp}}{\tau \mathbf{s}} \quad (6)$$

$$t_s = -\frac{\mathbf{t}}{\ln \Theta} \quad (7)$$

$$Q_0 = hS\,(T\,(max.\ NPs) - T\,(max.\ water)\,) \quad (8)$$

Where h is the heat transfer coefficient; S is the surface area; $T_{max,\ NPs}$ and $T_{max,\ water}$ refer to the maximum temperature of aqueous solution with and without PTA, respectively; I is the 808-nm laser power; A_λ is the absorbance of the PTA at 808 nm; m is the mass (1.0 g) and C_p is the heat capacity [4.2 J $(g\ ^\circ C)^{-1}$] of water; Θ is the dimensionless driving force temperature; T_{amb} is the ambient temperature.; τs is the time constant of an aqueous solution containing PTA. Based on the reported method by Roper and co-workers, the photothermal efficiency of GQDs-Fe/Bi NPs was calculated to be ~ 31.88% (Fig. 6F). The our efficiency value was comparable to the efficiency of pure Bi (30–32%) [2,12,20] and Bi compounds, e.g. the Bi2Se3 nanoplate (~ 34.7%) [26], the Bi_2Se_3 nanoscale spherical-sponge (~ 31.1%) [31], and the Bi2S3 nanorods (~ 28.1%) [4], and much higher than that of the widely-used Au nanorods (~ 21%) and Au nanoshells (~ 13%) [28]. In summary, the excellent photothermal effect and photostability propose that the as-synthesized nanoparticles based on bismuth are suitable PTAs.

3.1.5. *In vitro photothermal ablation of cancerous cells*

The excellent photothermal property of the GQDs-Fe/Bi NPs was encouraging to study their effectiveness for the treatment of cancer cells. The dead cells to live one's percentage was measured in each group with different treatments (e.g. only laser, treated with GQDs-Fe/Bi NPs + laser) after 10 min irradiation. According the cell images acquired under different treatment (Fig. 7**A-B**), almost no dead cells were observed in the groups irradiated with only NIR laser than the control ones, while, MCF-7 and HeLa cells were considerably killed in the presence of NPs. The quantified results showed that the co-treatment of GQDs-Fe/Bi NPs with NIR laser irradiation was able to significantly kill the cancer cells (**$p < 0.05$;** Fig. 7C). In contrast, the laser irradiation only had no obvious effect on the survival reduction of both types of cell lines than those in the control one. The cell-killing effect mediated by the co-treatment of GQDs-Fe/Bi NPs and laser followed a concentration-dependent manner. Additionally, after photothermal treatment, Annexin-V-FITC/PI method was used to detection of cell death mechanism in MCF-7 cells (Fig. 8C). In the group treated with the only laser, the cell apoptosis or necrosis effect was found to be negligible with a small rate of 8.67%. While, the co-killing effect of the GQDs-Fe/Bi NPs and laser irradiation successfully increased dose-dependent the irreversible cell damage rate. The sum of early and late apoptosis for MCF-7 cells co-treated with 25 $\mu g.mg^{-1}$ concentration of Bi active

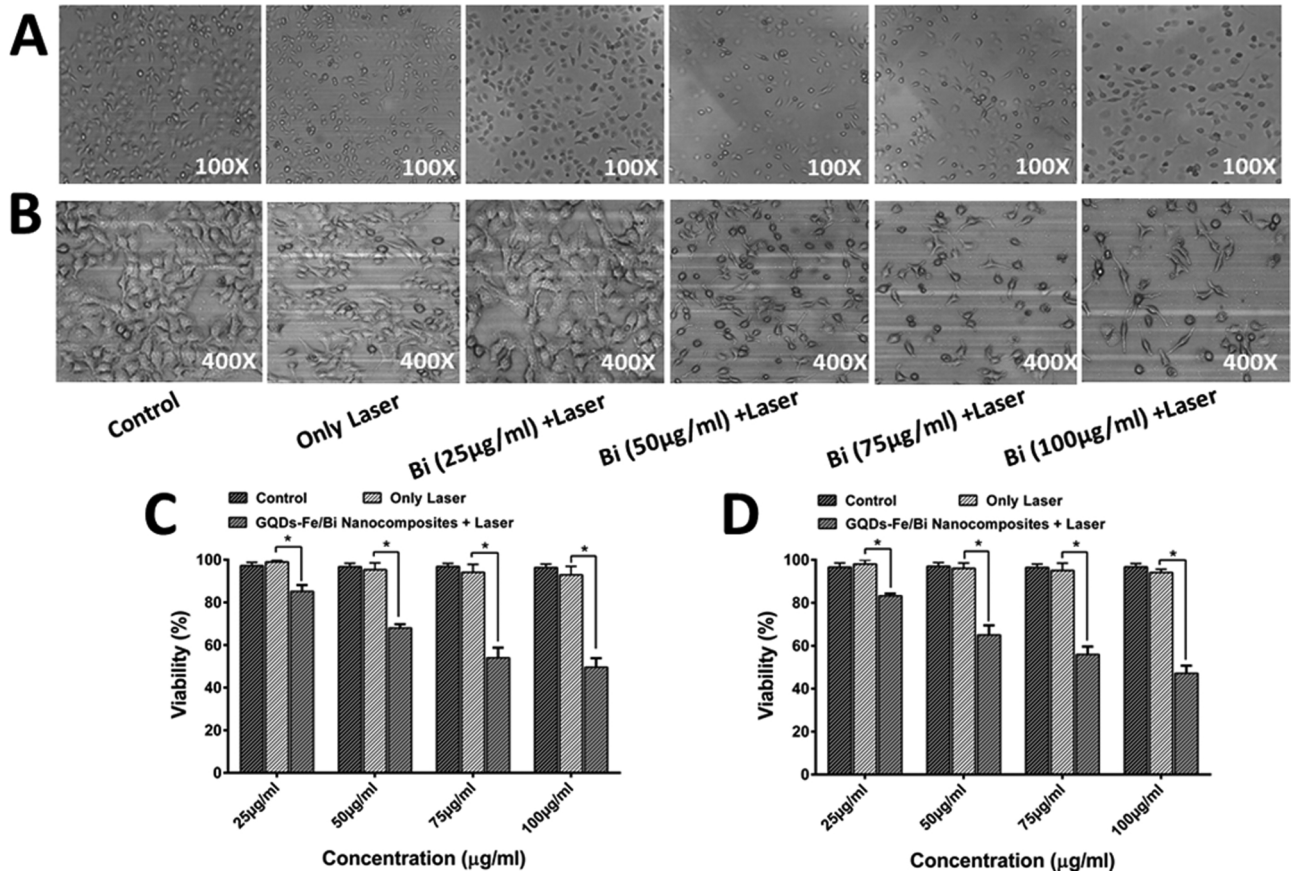

Fig. 7. Photothermal therapy effect: Optical microscopy images of **A)** HeLa and **B)** MCF-7 cells with different treatment; Cell viability of **C)** HeLa and **D)** MCF-7 cells after incubation with different concentrations of GQDs-Fe/Bi NPs under 808 nm NIR laser irradiation. The results are represented as mean ± SD. (*$p < 0.05$). SD: standard deviation.

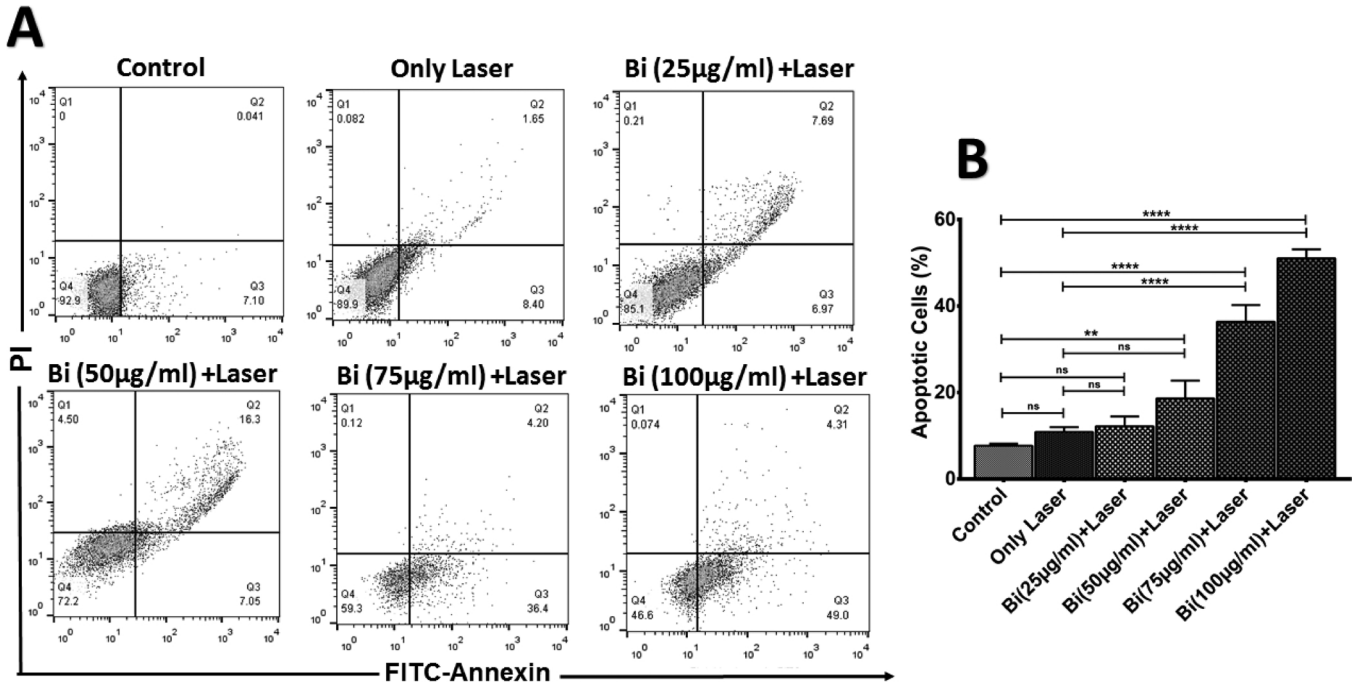

Fig. 8. A) Flow cytometric profiles of MCF-7 cells co-treated with irradiation laser and different concentrations of GQDs-Fe/Bi NPs (Q4: viable cells in bottom left (Annexin V-/PI), Q3: early apoptotic cells in bottom right (Annexin V + /PI-), Q2: late apoptotic cells in top right (Annexin V + / P +), and Q1: necrotic cells in top left (Annexin V-/PI +)). The results are represented as mean ± SD. (**$p < 0.0010$, ****$p < 0.0001$). SD: standard deviation.

metal in GQDs-Fe/Bi NPs was calculated to be 10.05%. In contrast, the proportion of apoptosis significantly increased to 23.35%, 40.6% and 53.31% after co-treatment of MCF-7 cells with concentrations of 50, 75 and 100 μg Bi.mg^{-1}, respectively (**p < 0.0010, p < 0.0001; Fig. 8C).

As a result, the GQDs-Fe/Bi NPs mediated photothermal effect induced permanent damage and dysfunctionality within MCF-7 cells.

4. Conclusion

In summary, the GQDs-Fe/Bi NPs have been successfully developed as a high-performance theranostic agent. The GQDs coating of Fe/Bi NPs not only resulted in the excellent dispersion of NPs but also effectively improved their photostability. In the NIR region, the GQDs-Fe/Bi NPs hold a broad and high absorption and a photo-to-thermal conversion efficiency as high as ~ 31.88%. Therefore, the co-treatment of the cancer cells with GQDs-Fe/Bi NPs and NIR irradiation show a high-inhibitory effect on cell proliferation, while there is no such result after treatment with irradiation alone. Thanking to the large attenuating capability of Bi element, the GQDs-Fe/Bi NPs can perform a high-contrast CT imaging with a CT enhancement efficiency of 44.4 HU. mM^{-1}, which is much higher than that of commercially clinical iodine-based. Also, they demonstrate high performance on MR imaging with respect to the superparamagnetic property of Fe NPs, with a transverse relaxation time (T_2) shorting capability of 62.34 mM^{-1}.s^{-1}. Such a multifunctional nanohybrid combining advantages of high-contrast CT/MR bimodal imaging and effective photothermal treatment offers a promising route in the field of cancer therapy.

Acknowledgments

The authors would like to thank Drug Applied Research Center, Tabriz University of Medical Sciences for its financial support of this project [Grant No. 94/2-5/10].

Appendix A. Supplementary data

Supplementary material related to this article can be found, in the online version, at doi:https://doi.org/10.1016/j.pdpdt.2018.10.021.

References

[1] J.A. Barreto, et al., Nanomaterials: applications in cancer imaging and therapy, Adv. Mater. 23 (12) (2011).
[2] P. Lei, et al., Ultrafast synthesis of ultrasmall poly (Vinylpyrrolidone)-protected Bismuth Nanodots as a multifunctional theranostic agent for in vivo dual-modal CT/Photothermal-imaging-guided photothermal therapy, Adv. Funct. Mater. 27 (35) (2017).
[3] J. Li, et al., Topological insulator bismuth selenide as a theranostic platform for simultaneous cancer imaging and therapy, Sci. Rep. 3 (2013).
[4] Z. Li, et al., Multimodal imaging-guided antitumor photothermal therapy and drug delivery using bismuth selenide spherical sponge, ACS Nano 10 (10) (2016) 9646–9658.
[5] L. Jing, et al., Prussian blue coated gold nanoparticles for simultaneous photoacoustic/CT bimodal imaging and photothermal ablation of cancer, Biomaterials 35 (22) (2014) 5814–5821.
[6] X. Huang, et al., Cancer cell imaging and photothermal therapy in the near-infrared region by using gold nanorods, J. Am. Chem. Soc. 128 (6) (2006) 2115–2120.
[7] G. Tian, et al., Multifunctional RbxWO3 nanorods for simultaneous combined chemo-photothermal therapy and Photoacoustic/CT imaging, Small 10 (20) (2014) 4160–4170.
[8] F.M. Kievit, M. Zhang, Cancer nanotheranostics: improving imaging and therapy by targeted delivery across biological barriers, Adv. Mater. 23 (36) (2011) H217–H247.
[9] X. Ma, Y. Zhao, X.-J. Liang, Theranostic nanoparticles engineered for clinic and pharmaceutics, Acc. Chem. Res. 44 (10) (2011) 1114–1122.
[10] P. Huang, et al., Biodegradable gold nanovesicles with an ultrastrong plasmonic coupling effect for photoacoustic imaging and photothermal therapy, Angew. Chemie Int. Ed. 52 (52) (2013) 13958–13964.
[11] Y. Zhang, et al., Hydrophilic graphene oxide/bismuth selenide nanocomposites for CT imaging, photoacoustic imaging, and photothermal therapy, J. Mater. Chem. B 5 (9) (2017) 1846–1855.
[12] Z. Li, et al., Biocompatible PEGylated bismuth nanocrystals:"All-in-one" theranostic agent with triple-modal imaging and efficient in vivo photothermal ablation of tumors, Biomaterials 141 (2017) 284–295.
[13] Z. Zhang, et al., Mesoporous silica-coated gold nanorods as a light-mediated multifunctional theranostic platform for cancer treatment, Adv. Mater. 24 (11) (2012) 1418–1423.
[14] W. Yin, et al., High-throughput synthesis of single-layer MoS2 nanosheets as a near-infrared photothermal-triggered drug delivery for effective cancer therapy, ACS Nano 8 (7) (2014) 6922–6933.
[15] Z. Zhang, et al., Near infrared laser-induced targeted cancer therapy using thermoresponsive polymer encapsulated gold nanorods, J. Am. Chem. Soc. 136 (20) (2014) 7317–7326.
[16] Z. Zha, et al., Polypyrrole hollow microspheres as echogenic photothermal agent for ultrasound imaging guided tumor ablation, Sci. Rep. 3 (2013) 2360.
[17] T. Liu, et al., Drug delivery with PEGylated MoS2 nano-sheets for combined photothermal and chemotherapy of cancer, Adv. Mater. 26 (21) (2014) 3433–3440.
[18] Y. Jin, et al., Encapsulating tantalum oxide into polypyrrole nanoparticles for X-ray CT/photoacoustic bimodal imaging-guided photothermal ablation of cancer, Biomaterials 35 (22) (2014) 5795–5804.
[19] K. Dong, et al., Hydrophobic anticancer drug delivery by a 980 nm laser-driven photothermal vehicle for efficient synergistic therapy of cancer cells in vivo, Adv. Mater. 25 (32) (2013) 4452–4458.
[20] X. Yu, et al., Ultrasmall semimetal nanoparticles of bismuth for dual-modal computed tomography/photoacoustic imaging and synergistic thermoradiotherapy, ACS Nano 11 (4) (2017) 3990–4001.
[21] L. Cheng, et al., PEGylated WS2 nanosheets as a multifunctional theranostic agent for in vivo dual-modal CT/photoacoustic imaging guided photothermal therapy, Adv. Mater. 26 (12) (2014) 1886–1893.
[22] Z. Gu, et al., Recent advances in design and fabrication of upconversion nanoparticles and their safe theranostic applications, Adv. Mater. 25 (28) (2013) 3758–3779.
[23] Q. Tian, et al., Sub-10 nm Fe3O4@ Cu2–x S core–Shell nanoparticles for dual-modal imaging and photothermal therapy, J. Am. Chem. Soc. 135 (23) (2013) 8571–8577.
[24] G.A. Sotiriou, et al., Photothermal killing of Cancer cells by the controlled plasmonic coupling of silica-coated Au/Fe2O3 nanoaggregates, Adv. Funct. Mater. 24 (19) (2014) 2818–2827.
[25] J. Yu, et al., Multifunctional Fe5C2 nanoparticles: a targeted theranostic platform for magnetic resonance imaging and photoacoustic tomography-guided photothermal therapy, Adv. Mater. 26 (24) (2014) 4114–4120.
[26] Z. Li, et al., Multifunctional bismuth selenide nanocomposites for antitumor thermo-chemotherapy and imaging, ACS Nano 10 (1) (2015) 984–997.
[27] G. Song, et al., Core–shell MnSe@ Bi2Se3 fabricated via a cation exchange method as novel nanotheranostics for multimodal imaging and synergistic thermoradiotherapy, Adv. Mater. 27 (40) (2015) 6110–6117.
[28] H. Ke, et al., Gold nanoshelled liquid perfluorocarbon nanocapsules for combined dual modal ultrasound/CT imaging and photothermal therapy of cancer, Small 10 (6) (2014) 1220–1227.
[29] L. Cheng, et al., FeSe2-decorated Bi2Se3 nanosheets fabricated via cation exchange for chelator-free 64Cu-labeling and multimodal image-guided photothermal-radiation therapy, Adv. Funct. Mater. 26 (13) (2016) 2185–2197.
[30] R. Dou, et al., The polyvinylpyrrolidone functionalized rGO/Bi 2 S 3 nanocomposite as a near-infrared light-responsive nanovehicle for chemo-photothermal therapy of cancer, Nanoscale 8 (22) (2016) 11531–11542.
[31] J. Liu, et al., Bismuth sulfide nanorods as a precision nanomedicine for in vivo multimodal imaging-guided photothermal therapy of tumor, ACS Nano 9 (1) (2015) 696–707.
[32] F. Mao, et al., Ultrasmall biocompatible Bi2Se3 nanodots for multimodal imaging-guided synergistic radiophotothermal therapy against cancer, ACS Nano 10 (12) (2016) 11145–11155.
[33] Y. Wang, et al., BSA-mediated synthesis of bismuth sulfide nanotheranostic agents for tumor multimodal imaging and thermoradiotherapy, Adv. Funct. Mater. 26 (29) (2016) 5335–5344.
[34] X.D. Zhang, et al., Metabolizable Bi2Se3 nanoplates: biodistribution, toxicity, and uses for cancer radiation therapy and imaging, Adv. Funct. Mater. 24 (12) (2014) 1718–1729.
[35] S. Badrigilan, et al., Graphene quantum dots-coated bismuth nanoparticles for improved CT imaging and photothermal performance, Int. J. Nanosci. (2018), https://doi.org/10.1142/S0219581X18500436.
[36] J.P. Naik, P. Sutradhar, M. Saha, Molecular scale rapid synthesis of graphene quantum dots (GQDs), J. Nanostructure Chem. 7 (1) (2017) 85–89.
[37] A.J.L. Villaraza, A. Bumb, M.W. Brechbiel, Macromolecules, dendrimers, and nanomaterials in magnetic resonance imaging: the interplay between size, function, and pharmacokinetics, Chem. Rev. 110 (5) (2010) 2921–2959.
[38] S. Veintemillas-Verdaguer, et al., Bismuth labeling for the CT assessment of local administration of magnetic nanoparticles, Nanotechnology 26 (13) (2015) 135101.
[39] P.C. Naha, et al., Dextran coated bismuth–iron oxide nanohybrid contrast agents for computed tomography and magnetic resonance imaging, J. Mater. Chem. B 2 (46) (2014) 8239–8248.
[40] Y. Li, et al., A cation-exchange controlled core–shell MnS@ Bi 2 S 3 theranostic

platform for multimodal imaging guided radiation therapy with hyperthermia boost, Nanoscale 9 (38) (2017) 14364–14375.
[41] H. Cai, et al., Facile assembly of Fe 3 O 4@ Au nanocomposite particles for dual mode magnetic resonance and computed tomography imaging applications, J. Mater. Chem. 22 (30) (2012) 15110–15120.
[42] X. He, et al., Lectin-conjugated Fe2O3@ Au core@ shell nanoparticles as dual mode contrast agents for in vivo detection of tumor, Mol. Pharm. 11 (3) (2014) 738–745.
[43] A.L. Brown, et al., Synthesis, X-ray opacity, and biological compatibility of ultra-high payload elemental bismuth nanoparticle X-ray contrast agents, Chem. Mater. 26 (7) (2014) 2266–2274.
[44] J. Choi, et al., Physicochemical characterization and in V itro hemolysis evaluation of silver nanoparticles, Toxicol. Sci. 123 (1) (2011) 133–143.
[45] P. Lei, et al., Ultrafast synthesis of ultrasmall poly (Vinylpyrrolidone)-protected Bismuth Nanodots as a multifunctional theranostic agent for in vivo dual-modal CT/Photothermal-imaging-guided photothermal therapy, Adv. Funct. Mater. 27 (35) (2017) 1702018.